Available online at www.sciencedirect.com

ScienceDirect

Procedia Manufacturing 48 (2020) 443–451

Procedia MANUFACTURING

www.elsevier.com/locate/procedia

48th SME North American Manufacturing Research Conference, NAMRC 48 (Cancelled due to COVID-19)

Cutting force and stability prediction for inserted cutters

Michael Gomez[a,b], Timothy No[a], Scott Smith[b], and Tony Schmitz[a,b]*

[a]*University of Tennessee, Knoxville, 1512 Middle Dr., Knoxville, TN 37996, USA*
[b]*Energy and Transportation Science Division, Oak Ridge National Laboratory, Oak Ridge, TN 37830, USA*

* Corresponding author. Tel.: +1-865-974-6141. *E-mail address:* tony.schmitz@utk.edu

Abstract

This paper presents an approach for inserted end/face mill force and stability predictions using a reverse engineering approach. Structured light scanning is implemented to identify the spatial coordinates of the points that define the multiple insert cutting edges. These points are analyzed to extract the cutting edge radius and angle values, which are then incorporated in a time domain simulation that predicts cutting force and tool/workpiece deflection for user-selected operating parameters. Good agreement between predicted and measured cutting forces is first demonstrated. The process stability is then predicted using the validated force model and measured structural dynamics. Observations about the stability dependence on insert geometry are finally presented for a selected end mill.

Keywords: Machining; force; stability; inserted end mill; structured light

1. Introduction*

Machining is used to produce a wide variety of discrete components across a broad range of industries, including aerospace, automotive, defense, and others. Advantages of machining include net shape production of complex geometries in nearly any material with the desired geometry and surface finish for functional and mating surfaces. A challenge is the need to select optimized machining conditions for maximum profit or highest performance, for example. This selection is complicated by the wide array of available cutting tools and workpiece materials and the corresponding variation in the structural dynamics with the selected cutting tool-holder-spindle-machine-workpiece-fixturing combination. One common geometry is inserted cutting tools, where hard inserts (carbide or ceramic, for example) are clamped to a steel tool body. This enables the cutting edges to be conveniently replaced at periodic intervals as wear progresses. It also tends to reduce tooling costs since the more expensive material is limited to the insert and the tool body may be produced from a lower cost material.

Nomenclature

r	radius of point on end mill cutting edge
ϕ	angle of point on end mill cutting edge
z	position along end mill axis
$\Delta\phi$	angular resolution in time domain simulation
SR	steps per revolution in time domain simulation
RO	runout for point on end mill cutting edge
F_t	tangential component of cutting force
F_n	normal component of cutting force

10.1016/j.promfg.2020.05.067

k_{tc}	cutting coefficient for tangential component
k_{te}	edge coefficient for tangential component
k_{nc}	cutting coefficient for normal component
k_{ne}	edge coefficient for normal component
m	modal mass
c	modal viscous damping coefficient
k	modal stiffness
x	feed direction for end milling operation
y	perpendicular direction to x in the cut plane
$M1$	stability metric for once-per-revolution sampling
$M2$	stability metric for period-2 bifurcations
x_s	once-per-revolution sampled x displacements
x_{2s}	once-per-two revolution sampled x displacements
N	number of samples

2. Background

Several authors have modeled the performance of inserted cutters. Fu *et al.* predicted the forces in face milling for various cutting conditions and cutter geometries [1]. Kim and Ehmann simulated the static and dynamic cutting forces in face milling [2]. Zheng *et al.* modeled face milling as the simultaneous action of multiple single point cutting tools [3]. Engin and Altintas presented a generalized inserted cutter model for predicting cutting force, vibration, surface finish, and stability in milling, where the cutting edge locations were defined mathematically [4-5]. Franco studied surface roughness for round insert cutting tools [6]. Wiederkehr *et al.* presented a point-based method for modeling rotating tool and predicting forces, tool deflections, and surface location errors during five-axis machining [7].

These inserted end/face mill modeling efforts are augmented by serrated edge cutter performance simulation activities also available in the literature. The two are similar in that both address tool geometries that depart from the equally spaced, helical cutting edges for standard end mills. Wang and Yang [8] modeled a cylindrical roughing end mill with sinusoidal cutting edges. Merdol and Altintas [9] described the serration profile by fitting points along a cubic spline projected on the helical flutes and implemented this geometric model in a time domain milling model. Dombovari *et al.* [10] used the semi-discretization method to analyze the stability of serrated end mills; see also [11, 12]. Koca and Budak [13] optimized the serration waveform shape to reduce milling forces and increase stability. Grabowski *et al.* [14] calculated cutting forces for serrated endmills. Tehranizadeh and Budak [15] proposed a genetic algorithm to optimize serration designs.

This paper builds on these previous efforts by incorporating the measured edge coordinates for an inserted end mill directly in a time domain simulation to predict time-dependent forces and displacements during machining. In this case, an *a priori* (manufacturer-specified) geometric model of the end or face mill is not required because the geometry is measured using structured light scanning.

3. Inserted end mill measurements

To model the performance of inserted end and face mills without requiring a model of the tool geometry from the manufacturer, scanning metrology is leveraged in this study. Structured light, or fringe, projection is applied to collect point clouds from the complex inserted tool surfaces. While many commercial options are available, the GOM ATOS Compact Scan system was used for this research. The measurements proceeded by first preparing the inserted end mill surface using a removable anti-glare coating and attaching reference targets to the shank surface to enable multiple measurements to be stitched together and generate the solid model. Second, multiple scans were completed to obtain the point cloud and 3D model [16-17].

The procedure used to extract the edge coordinates from the solid model included four steps. First, using the best fit cylinder to the tool shank and the inserted end's extreme point, the origin was established on the tool's center line. Second, the points located on the insert cutting edges were selected. This step required manual manipulation within the GOM software. The average point spacing on the three cutting edges for the top row of inserts in Fig. 1 was 57 µm, while the minimum spacing was 0.1 µm and the maximum was 267 µm. Third, the radius, r, and angle, ϕ, for each edge point was calculated in the local coordinate system. The teeth angles were normalized to a selected tooth and constrained to values between 0 and 360 deg; the z value was retained to obtain a triplet, $\{r, \phi, z\}$ for each point. Fourth, because the point density was higher than required for the time domain simulation, linear interpolation was used to obtain the triplet for axial slices located every 0.1 mm over the full cutting length; see Fig. 1, which displays the edge points for the Kennametal indexable, square shoulder, helical end mill (part number 3746099, three teeth, 31.8 mm shank and cut diameters, 111 mm overall length, and 44.8 mm maximum cut depth). The 15 inserts (three "teeth" with five inserts each) were Kennametal EP1008 HD Grade KC725M carbide milling inserts with a TiN/TiCN/TiN coating (part number 3641734, 3.8 mm thickness, and 0.8 mm corner radius).

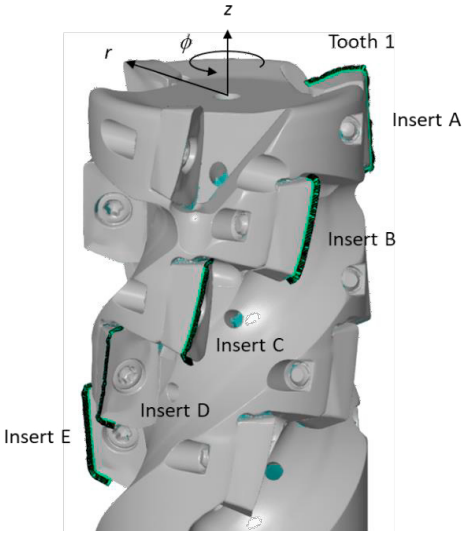

Fig. 1. Scan and edge coordinates for one tooth on the indexable, square shoulder, helical end mill (31.8 mm shank and cut diameters, three teeth, 15 inserts total).

Example insert angle results are provided in Fig. 2. It is observed that the inserts are equally spaced at nominally 120 deg around the end mill periphery and that the angular offset between rows A and B (71 deg) differs from the offsets between rows B and C, C and D, and D and E (46 deg). Radius results are displayed in Fig. 3. It is seen that each insert has a characteristic "U" shape with a smaller radius at the center and higher radii at the ends. The total variation in radii (excluding the rounded edges) across all 15 inserts is 135 µm. The runout contributes to the final force profile and must be incorporated for accurate force predictions.

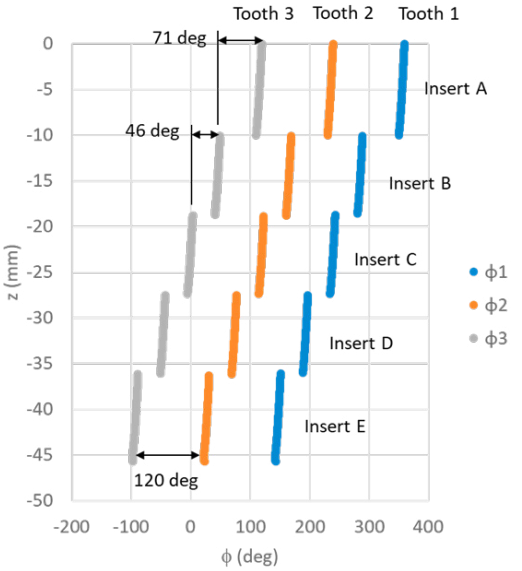

Figure 2: Insert angles, ϕ, for the three teeth calculated from the edge coordinates identified in Fig. 1.

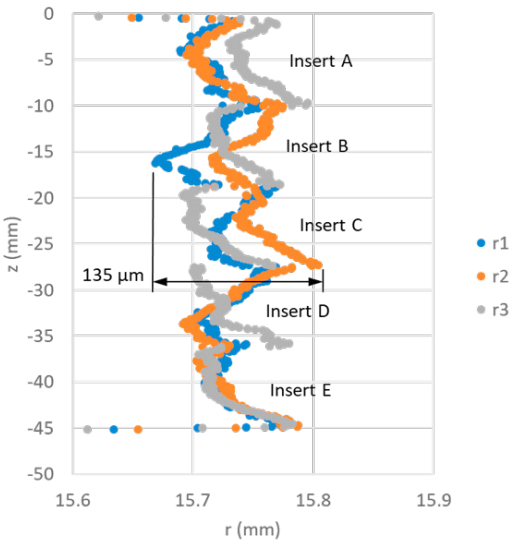

Fig. 3. Insert radii obtained from the edge coordinates identified in Fig. 1.

The helix angles are described in Fig. 4. There are three primary angles. First, each insert is inclined with a mean helix angle of 14.7 deg. Second, two "global" helix angles can be identified. The first is due to the 71 deg angular offset between rows A and B. By unwrapping the cutter's periphery into a planar representation, the associated helix angle was obtained from the slope of a line that connected the tips of the two inserts. This helix angle is 62.6 deg. The second helix angle is provided by the 46 deg angular offset between the other pairs of insert rows and the corresponding best fit line's slope. This angle is 55.5 deg.

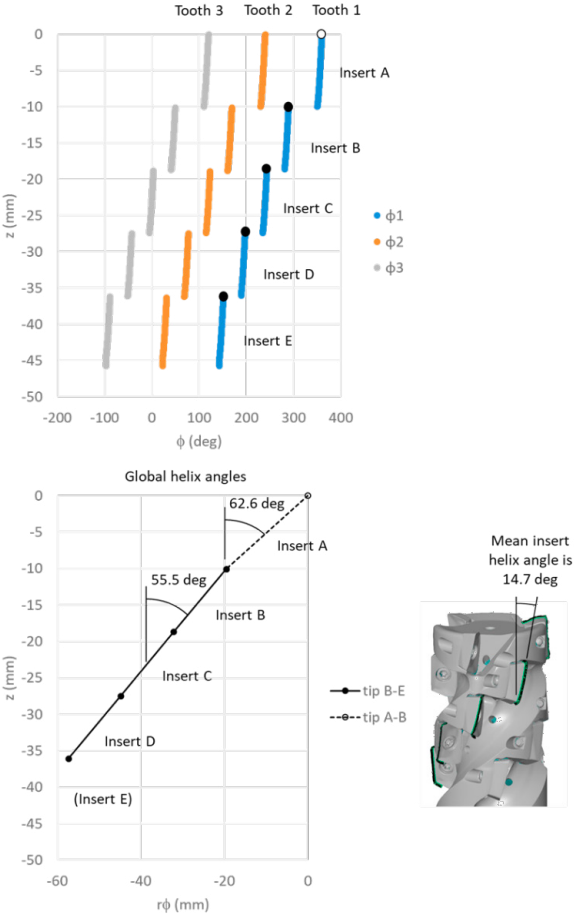

Fig. 4. (Top) Tip points on each insert were selected to calculate the global helix angles. The points are shown for tooth 1. (Bottom left) Global helix angles; two are identified due to the different angular offsets between rows A and B and the other pairs. (Bottom right) Mean helix angle for each insert.

4. Simulation description

Time domain simulation enables numerical solution of the coupled, time delay equations of motion for milling in small time steps [18]. It is well suited to incorporating the inherent complexities of milling dynamics, including complicated tool geometries (runout of the cutter teeth, non-uniform teeth spacing, and variable helix) and the nonlinearity that occurs if the tooth leaves the cut due to large magnitude vibrations. The simulation applied here is based on the regenerative force, dynamic deflection model described by Smith and Tlusty [19]. As opposed to analytical or semi-analytical stability maps that provide a global picture of the stability behavior, time domain simulation provides information regarding the local cutting force and vibration behavior for the selected cutting conditions.

The simulation used in this study is described in the following paragraphs; it was previously validated for serrated cutter geometries [16-17].

The time domain simulation directly incorporated the measured tooth angles and radius variation displayed in Figs. 2 and 3. For the tooth angles, the measured angles from the scanned edge were arranged in an array, where the columns were the individual teeth and the rows were the z locations (in steps of 0.1 mm). A row array of closely spaced tooth angles for use in the time domain simulation was then defined. The resolution in this array was: $\Delta\phi = 360/SR$, where SR is the number of steps per revolution in the simulation.

Once this array was defined, the measured tooth angles were specified in an index array with each entry given by the ratio $\phi/\Delta\phi$ rounded to the nearest integer, where ϕ is the measured angle of the tooth at the selected z location. This index array was then used to specify the angle of any tooth at any z location by identifying the nearest preselected value from the closely spaced tooth angle array for use in the simulation. The reason for this approach is that the current chip thickness in milling depends not only on the commanded chip thickness and current vibration, but also the surface left by the previous teeth at the current tooth angle. To be able to do so conveniently, this information was organized according to specified tooth angles.

The radius variation for each insert was included as runout, RO. The z-dependent RO values for each of the 15 inserts were also arranged in an array, where the columns were the individual teeth (i.e., the collection of five inserts) and the rows were the z locations (again in steps of 0.1 mm). All RO values were normalized to the maximum radius from all 15 inserts, which yielded negative RO values. A negative RO value reduces the chip thickness for the current tooth, but leaves behind material that the next tooth must remove (and therefore increases that chip thickness).

Two other data organization requirements were: 1) the surface that was left behind by the current tooth; and 2) the commanded chip thickness. To keep track of the previously machined surface, another array was defined that recorded the surface location in the tool's normal direction for each simulation time step. The columns of this matrix were the number of steps per revolution and the rows were the z locations. The influence of runout on subsequent chip thickness values was captured in this matrix. Because there were variations in the tooth angles from one insert to the next, the commanded chip thickness was also modified to account for the actual tooth angle using the circular tooth path approximation. This approximation calculates the nominal chip thickness from the product of the feed per tooth and the sine of the tooth angle.

Given this information, the simulation proceeded as follows:

1. The instantaneous chip thickness, $h(t)$, was determined using the commanded chip thickness, runout, and vibration of the current and previous teeth at the selected tooth angle.
2. The cutting force components in the tangential, t, and normal, n, directions were calculated at each axial slice using a mechanistic approach:

$$F_t(t) = k_{tc} b h(t) + k_{te} b \quad (1)$$

$$F_n(t) = k_{nc} b h(t) + k_{ne} b \quad (2)$$

where b is the slice width (0.1 mm) and the cutting force coefficients are identified by the subscripts: t or n for direction; and c or e for cutting or edge effect. These forces were then summed over all axial slices engaged in the cut.

3. The summed force components were used to find the new displacements by numerical solution of the differential equations of motion in the x (feed) and y directions:

$$m_x \ddot{x} + c_x \dot{x} + k_x x = F_t(t)\cos\phi + F_n(t)\sin\phi \quad (3)$$

$$m_y \ddot{y} + c_y \dot{y} + k_y y = F_t(t)\sin\phi - F_n(t)\cos\phi \quad (4)$$

where m is the modal mass, c is the modal viscous damping coefficient, and k is the modal stiffness. The subscripts identify the direction and multiple degrees-of-freedom in each direction can be accommodated by summing the modal contributions.

4. The tool rotation angle was incremented by adding one to each entry in the tooth angle index array and the process was repeated.

A simulation flowchart is provided in Fig. 5.

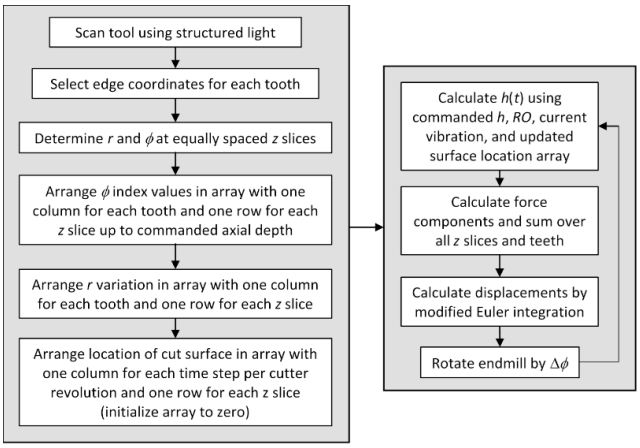

Fig. 5. Time domain simulation flowchart. (Left) setup information. (Right) simulation steps.

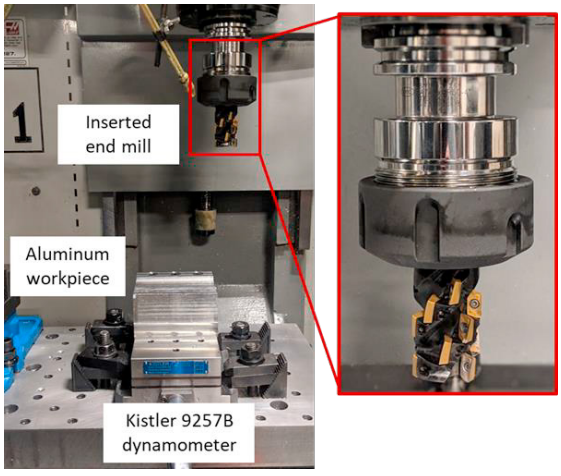

Figure 6: Experimental setup for milling force measurement.

5. Cutting force comparison

The experimental setup for milling force measurement with the inserted end mill is shown in Fig. 6. Trials were completed on a Haas TM-1 three-axis computer numerically controlled (CNC) milling machine. The 6061-T6 aluminum workpiece was mounted on a cutting force dynamometer (Kistler 9257B) and the endmill was clamped in an ER50 collet holder and inserted in the CAT-40 spindle interface. Tests were performed at axial depths of cut from 5 mm to 20 mm. The commanded feed per tooth for these down (climb) milling experiments was 100 µm/tooth, the spindle speed was 3550 rpm, and the radial depth of cut was 1.59 mm (5% radial immersion).

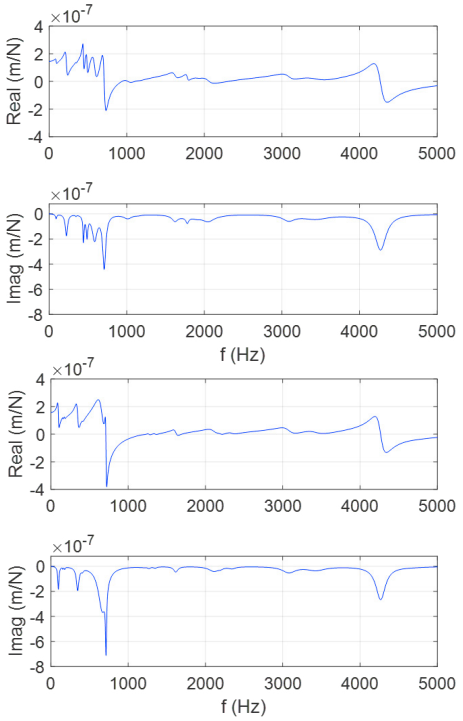

Fig. 7. Measured FRFs for *x* (top) and *y* (bottom) directions.

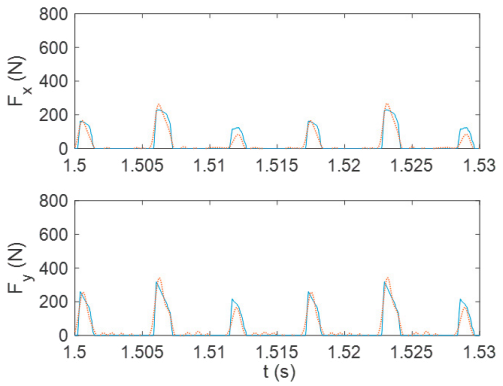

Fig. 8. Comparison of measured (red dotted line) and predicted (blue solid line) forces for the *x* (feed) and *y* directions; axial depth is 5 mm.

In a second set of tests, the axial depth was held constant at 5 mm and the feed per tooth was varied from 25 µm to 100 µm. The same spindle speed and radial depth were used. The tool and workpiece frequency response functions, or FRFs, were measured by impact testing, where an instrumented hammer is used to excite the structure and the response is measured using a linear transducer (a low-mass accelerometer for this research); see Fig. 7 for the combined FRFs in the *x* and *y* directions. Modal fitting was applied to extract the modal parameters for the time domain simulation; see Appendix A.

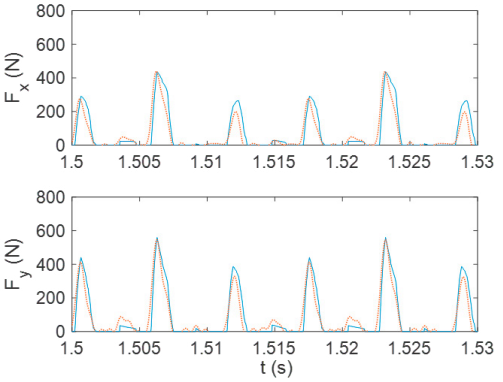

Fig. 9. Comparison of measured (red dotted line) and predicted (blue solid line) forces for the *x* (feed) and *y* directions; axial depth is 10 mm.

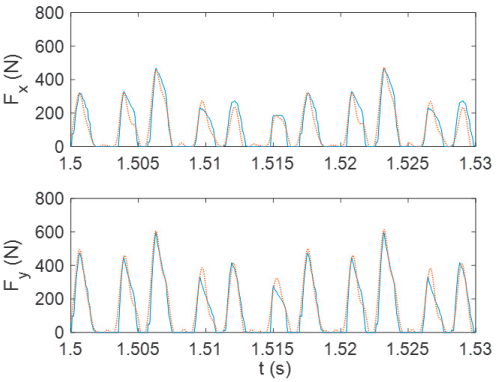

Fig. 10. Comparison of measured (red dotted line) and predicted (blue solid line) forces for the *x* (feed) and *y* directions; axial depth is 15 mm.

Measured and predicted *x* (feed) and *y* direction force values for b = {5, 10, 15, and 20} mm are shown in Figs. 8-11, where the cutting force coefficients for Eqs. 1 and 2 were: k_{tc} = 600×10^6 N/m^2, k_{nc} = 200×10^6 N/m^2, k_{te} = 25×10^3 N/m, and k_{ne} = 25×10^3 N/m. These values were based on prior cutting tests and experience with 6061-T6 aluminum. Good agreement is observed for all four axial depths, where the blue (solid) line is predicted and the red (dotted) line is measured. For the 5 mm axial depth, cutting with a single row of inserts (A in Fig. 1) occurs. Two revolutions of data are displayed, so six peaks are observed – one for each of the three inserts for both revolutions. At 10 mm, the second row of inserts (B in Fig. 1) begins to engage so additional peaks emerge and the force level is increased overall. At 15 mm, insert row B is fully engaged. For the 20 mm axial depth, insert row C begins cutting. The complicated, uneven force profiles in Figs. 8-11 are a product of both the inserted end mill geometry and runout.

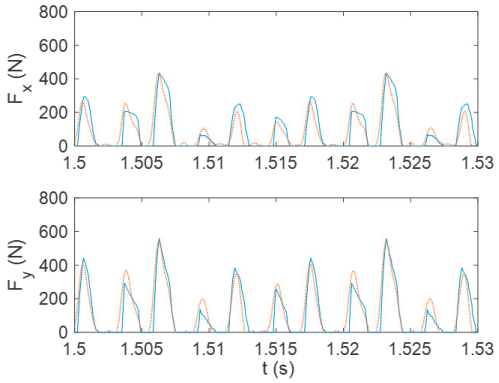

Fig. 11. Comparison of measured (red dotted line) and predicted (blue solid line) forces for the *x* (feed) and *y* directions; axial depth is 20 mm.

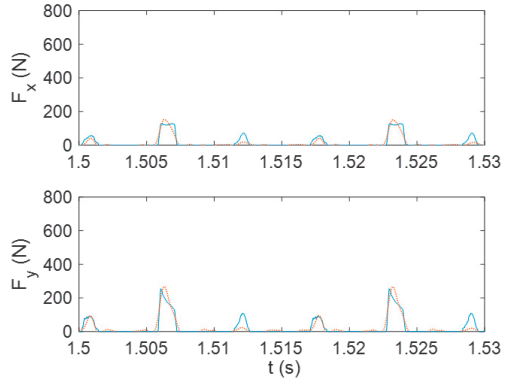

Fig. 12. Comparison of measured (red dotted line) and predicted (blue solid line) forces for the *x* (feed) and *y* directions; feed per tooth is 25 µm.

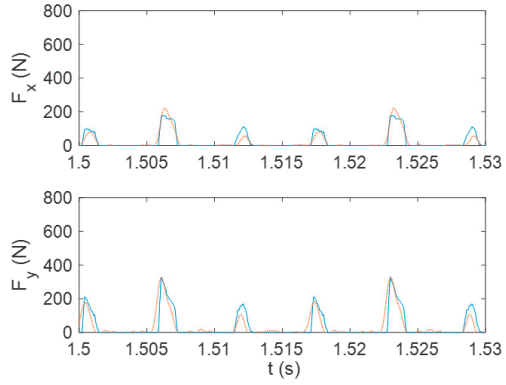

Fig. 13. Comparison of measured (red dotted line) and predicted (blue solid line) forces for the *x* (feed) and *y* directions; feed per tooth is 50 µm.

Measured and predicted *x* and *y* direction force values for feed per tooth values of {25, 50, 75, and 100} µm are displayed in Figs. 12-15. The axial (5 mm) and radial (1.58 mm) depths were fixed. Good agreement is again observed. For the constant 5 mm axial depth, cutting proceeds with only the row A inserts. As expected, the force level increases with feed, but the overall character does not change.

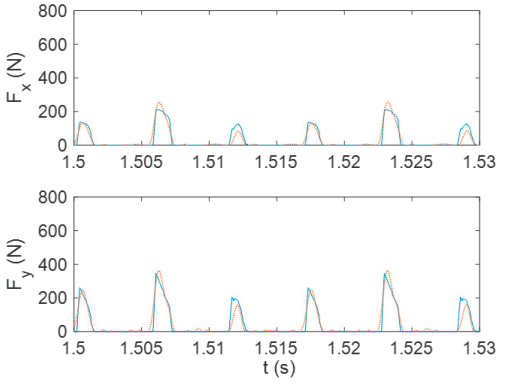

Fig. 14. Comparison of measured (red dotted line) and predicted (blue solid line) forces for the *x* (feed) and *y* directions; feed per tooth is 75 µm.

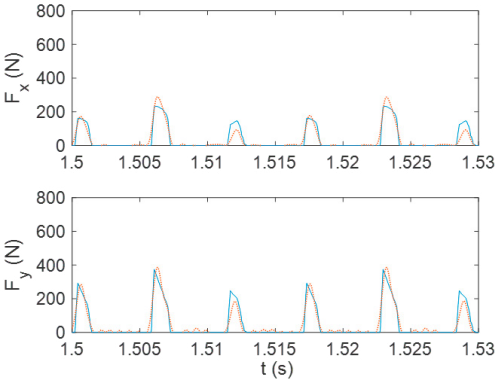

Fig. 15. Comparison of measured (red dotted line) and predicted (blue solid line) forces for the *x* (feed) and *y* directions; feed per tooth is 100 µm.

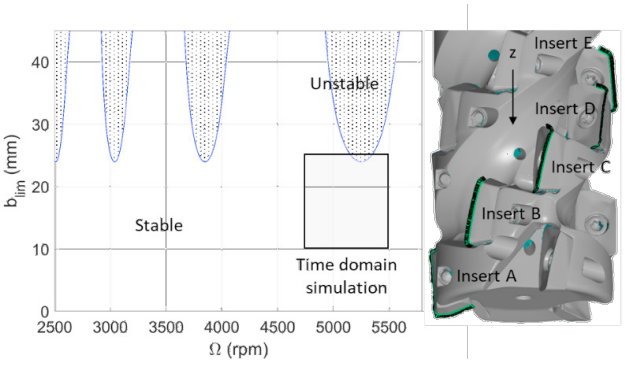

Fig. 16. Analytical stability limit, b_{lim}, expressed as a function of spindle speed, **Ω**. The relationship to the end mill geometry is shown by the solid model on the right. The range of spindle speeds and axial depths for the detailed time domain simulation grid is also identified.

6. Discussion

Given the validated force model, measured structural dynamics, and previously verified time domain simulation [16-17], the next activity was to examine the stability behavior of the inserted end mill. As a first step, the mean force, frequency domain analytical stability limit presented by Altintas and Budak was first computed [20]. The result is displayed in Fig.

16, where the end mill model is included to relate the insert locations to the limiting axial depth of cut, b_{lim}. To explore the stability behavior in greater detail, a grid of simulations was completed over the spindle speed-axial depth intervals identified in Fig. 16.

The stability behavior for each time domain simulation (4700 rpm to 5500 rpm in steps of 10 rpm and 10 mm to 25 mm in steps of 0.2 mm) was automatically determined by synchronous sampling, where stable behavior can be identified from the distribution of periodically sampled points. If the points repeat each revolution, then only forced vibration is present and the cut is stable. If they do not repeat, then either secondary Hopf or period-n (n = 2, 3, …) bifurcations are present. To distinguish between the alternatives automatically and qualitatively, the metrics described in [21-22] were employed. In this case, however, the sampling was completed once-per-spindle revolution rather than with each tooth period. This is because the behavior does not repeat from tooth-to-tooth, in general, even under stable cutting conditions due to the insert geometry. The metric, $M1$, for stable cutting was:

$$M1 = \frac{\sum_{i=2}^{N} |x_s(i) - x_s(i-1)|}{N}, \tag{5}$$

$$M2 = \frac{\sum_{i=2}^{N} |x_{s2}(i) - x_{s2}(i-1)|}{N} \tag{6}$$

where x_s is the vector of sampled x direction displacements and N is the number of samples. To interpret this metric, consider a stable cut where the behaviour repeats each revolution and the sampled points are nominally equal. The absolute value of the difference between subsequent points is then zero and their normalized sum remains zero. If the cut exhibits secondary Hopf bifurcation, on the other hand, the points do not repeat. The difference between subsequent points is then nonzero and, when the sum of the absolute values of these differences is calculated and normalized to the number of points, it is greater than zero. The metric is therefore nominally zero for a stable cut and large for an unstable cut.

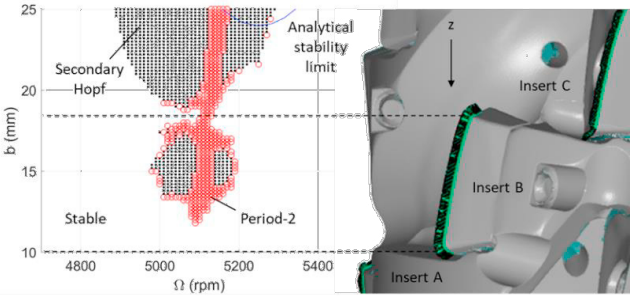

Fig. 17. Stability map obtained from time domain simulation. The inserted end mill solid model is included on the right to highlight the transition from cutting with inserts A and B only at axial depths below 18.6 mm to cutting with inserts A, B, and C at depths above this value.

The time domain simulation stability map is presented in Fig. 17. Three distinct regions are observed: stable (no symbols, $M1 < 1$ µm), secondary Hopf bifurcations (black dots, $M1 \geq 1$ µm), and period-2 bifurcations (red circles, $M2 < 1$ µm). The period-2 behavior was separately identified by modifying Eq. 5 as shown in Eq. 6 to obtain the $M2$ metric, where x_{s2} is the vector of x direction displacements sampled every second revolution and N is the number of samples. The analytical stability limit is also included in Fig. 17 for comparison. The inserted end mill geometry and 5% radial immersion (i.e., highly interrupted cutting) cause the process stability to diverge from the analytical prediction, which assumes equal teeth spacing along a single helix angle and considers only the mean value of the cutting force (i.e., the mean component of the Fourier series that represents the cutting force). Interesting behavior is observed in the simulation interval surrounding an axial depth of 18.6 mm. This region represents the transition from cutting with insert rows A and B only to cutting simultaneously with rows A, B, and C. Between rows B and C, there is a step change in the teeth spacing (see Fig. 2). This serves as a natural interruption to regeneration of waviness, a primary mechanism for self-excited vibration in milling, and increases the local stability.

To further explore this effect, individual simulation results are provided in Fig. 18. Poincaré maps, which plot the once-per-revolution sampled tool x direction displacement vs. velocity, are provided to clearly distinguish between the different instability types. In these maps, the blue line represents the continuous, time-dependent displacement-velocity trajectory and the red dots are the once-per-revolution samples. The stable result at {5060 rpm, 18.6 mm} displays just one dot. This means that the behavior repeats with each revolution because the same result is obtained each time and the multiple samples overlap (i.e., forced vibration). The period-2 results at 5120 rpm (both axial depths) displays two dots. This means that the behavior repeats every other revolution, alternating between the two discrete solutions. For the secondary Hopf bifurcation at {5060 rpm, 15 mm}, an elliptical distribution of sampled points appears. This is due to the presence of both the tooth passing frequency (and its harmonics) and the chatter frequency near the natural frequency that corresponds to the most flexible vibration mode (710 Hz for this experimental setup).

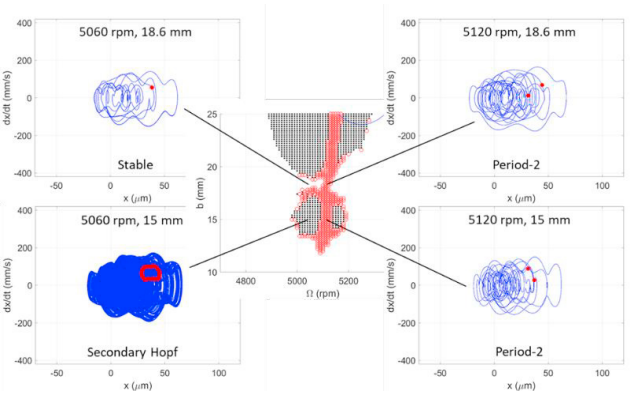

Fig. 18. Selected Poincaré maps for two spindle speeds (5060 rpm and 5120 rpm) and two axial depths (15 mm, inserts A and B only, and 18.6 mm, transition from A and B only to A, B, and C inserts cutting).

7. Conclusions

This paper provides a reverse engineering solution for modeling the behavior of inserted end/face mills. Structured light scanning was used to produce a solid model of an example inserted end mill. From this model, spatial coordinates for the points that define the insert cutting edges were extracted. The points were used to determine the cutting edge radius and angle at equally spaced points along the tool's axis. The actual cutting edge geometry was then incorporated directly in a time domain simulation that was used to predict cutting force and tool/workpiece deflection for user-selected operating parameters. Good agreement between predicted and measured cutting forces was obtained.

The validated simulation was next used to predict stability. A stability map was generated to observe the process behavior over a range of spindle speeds and axial depths of cut. Periodic sampling was employed to automatically identify stable and unstable cutting conditions. It was seen that the process stability is modified at the transition from cutting with two insert rows to three insert rows for the selected end mill.

Acknowledgements

The authors gratefully acknowledge financial support from the National Science Foundation (CMMI-1561221) and Oak Ridge National Laboratory.

References

[1] Fu, H.J., DeVor, R.E. and Kapoor, S.G., 1984. A mechanistic model for the prediction of the force system in face milling operations. Journal of engineering for industry, 106(1), pp.81-88.
[2] Kim, H.S. and Ehmann, K.F., 1993. A cutting force model for face milling operations. International Journal of Machine Tools and Manufacture, 33(5), pp.651-673.
[3] Zheng, H.Q., Li, X.P., Wong, Y.S. and Nee, A.Y.C., 1999. Theoretical modelling and simulation of cutting forces in face milling with cutter runout. International Journal of Machine Tools and Manufacture, 39(12), pp.2003-2018.
[4] Engin, S. and Altintas, Y., 2001. Mechanics and dynamics of general milling cutters: Part II: Inserted cutters. International Journal of Machine Tools and Manufacture, 41(15), pp.2213-2231.
[5] Altintas, Y. and Engin, S., 2001. Generalized modeling of mechanics and dynamics of milling cutters. CIRP Annals, 50(1), pp.25-30.
[6] Franco, P., Estrems, M. and Faura, F., 2004. Influence of radial and axial runouts on surface roughness in face milling with round insert cutting tools. International Journal of Machine Tools and Manufacture, 44(15), pp.1555-1565.
[7] Wiederkehr, P., Siebrecht, T., Baumann, J. and Biermann, D., 2018. Point-based tool representations for modeling complex tool shapes and runout for the simulation of process forces and chatter vibrations. Advances in Manufacturing, 6(3), pp.301-307.
[8] Wang, J.J.J. and Yang, C.S., 2003. Angle and frequency domain force models for a roughing end mill with a sinusoidal edge profile. International Journal of Machine Tools and Manufacture, 43(14), pp.1509-1520.
[9] Merdol, S.D. and Altintas, Y., 2004. Mechanics and dynamics of serrated cylindrical and tapered end mills. Journal of Manufacturing Science and Engineering, 126(2), pp.317-326.
[10] Dombovari, Z., Altintas, Y. and Stepan, G., 2010. The effect of serration on mechanics and stability of milling cutters. International Journal of Machine Tools and Manufacture, 50(6), pp.511-520.
[11] Dombovari, Z., Munoa, J. and Stepan, G., 2012. General milling stability model for cylindrical tools. Procedia CIRP, 4, pp.90-97.
[12] Stépán, G., Munoa, J., Insperger, T., Surico, M., Bachrathy, D. and Dombóvári, Z., 2014. Cylindrical milling tools: comparative real case study for process stability. CIRP Annals, 63(1), pp.385-388.
[13] Koca, R. and Budak, E., 2013. Optimization of serrated end mills for reduced cutting energy and higher stability. Procedia CIRP, 8, pp.570-575.
[14] Grabowski, R., Denkena, B. and Köhler, J., 2014. Prediction of process forces and stability of end mills with complex geometries. Procedia CIRP, 14, pp.119-124.
[15] Tehranizadeh, F. and Budak, E., 2017. Design of serrated end mills for improved productivity. Procedia CIRP, 58, pp.493-498.
[16] No, T., Gomez, M., Copenhaver, R., Uribe Perez, J., Tyler, C., and Schmitz, T., 2019. Force and stability modeling for non-standard edge geometry endmills. Journal of Manufacturing Science and Engineering, in production.
[17] No, T., Gomez, M., Copenhaver, R., Perez, J.U., Tyler, C. and Schmitz, T.L., 2019. Scanning and modeling for non-standard edge geometry endmills. Procedia Manufacturing, 34, pp.305-315.
[18] Schmitz, T.L. and Smith, K.S., 2019. Machining Dynamics: Frequency Response to Improved Productivity, 2nd Ed. Springer, New York, NY.
[19] Smith, K.S. and Tlusty, J., 1991. An overview of modeling and simulation of the milling process. ASME Journal of Engineering for Industry, 113(2), pp.169-175.
[20] Altintaş, Y. and Budak, E., 1995. Analytical prediction of stability lobes in milling. CIRP annals, 44(1), pp.357-362.
[21] Honeycutt, A. and Schmitz, T., 2016. A new metric for automated stability identification in time domain milling simulation. Journal of Manufacturing Science and Engineering, 138(7), pp.074501.
[22] Honeycutt, A. and Schmitz, T., 2017. Milling stability interrogation by subharmonic sampling. Journal of Manufacturing Science and Engineering, 139(4), pp.041009.

Appendix A. Modal parameters

The modal parameters obtained from fitting the measured FRFs for the tool and workpiece are provided in Table A1.

Table A1. Modal parameters for inserted end mill and workpiece.

End mill			
Direction	m (kg)	k (N/m)	c (N-s/m)
x	19.0	3.47×10^{7}	4160
x	16.8	1.3×10^{8}	1786
x	12.6	1.19×10^{8}	1978
x	2.94	4.00×10^{7}	1353
x	1.76	3.50×10^{7}	532.0
x	5.90	2.40×10^{8}	4853
x	1.77	2.23×10^{8}	4599
x	1.41	2.35×10^{8}	1612
x	0.97	3.65×10^{8}	1181
x	0.47	2.19×10^{8}	1370
x	0.12	8.66×10^{7}	132.7
y	10.6	5.05×10^{7}	2535
y	0.88	1.56×10^{7}	681.5
y	4.19	8.42×10^{7}	454.6
y	5.65	5.83×10^{8}	2308
y	1.99	3.51×10^{8}	2016
y	0.85	3.19×10^{8}	1091
y	0.86	3.98×10^{8}	1558
y	0.15	1.09×10^{8}	141.5
Workpiece			
Direction	m (kg)	k (N/m)	c (N-s/m)
x	380	1.23×10^{8}	49048
x	543	2.56×10^{9}	46908

x	42.0	2.19×10^{9}	23522
x	4.03	4.18×10^{8}	2272
x	7.51	9.40×10^{8}	2051
x	7.31	1.05×10^{9}	6239
x	7.28	1.37×10^{9}	13021
x	9.52	3.51×10^{9}	35388
x	9.06	4.26×10^{9}	15445
x	2.81	1.72×10^{9}	8033
y	78.9	2.95×10^{7}	49048
y	1055	1.00×10^{9}	46908
y	559	7.11×10^{8}	23522
y	94.5	6.20×10^{8}	2272
y	27.1	1.54×10^{9}	2051
y	47.7	3.04×10^{9}	6239
y	39.1	2.81×10^{9}	13021
y	15.3	2.90×10^{9}	35388
y	7.10	1.54×10^{9}	15445
y	2.60	2.22×10^{9}	8033